In Situ GISAXS Study of Gold Film Growth on Conducting Polymer Films

Gunar Kaune,[†] Matthias A. Ruderer,[†] Ezzeldin Metwalli,[†] Weinan Wang,[†] Sebastien Couet,[‡] Kai Schlage,[‡] Ralf Röhlsberger,[‡] Stephan V. Roth,[‡] and Peter Müller-Buschbaum*[,†]

Physik Department LS E13, Technische Universität München, James-Franck-Strasse 1, 85747 Garching, Germany, and HASYLAB at DESY, Notkestrasse 85, 22603 Hamburg, Germany

ABSTRACT The growth of a thin gold film on a conducting polymer surface from nucleation to formation of a continuous layer with a thickness of several nanometers is investigated in situ with grazing incidence small-angle X-ray scattering (GISAXS). Time resolution is achieved by performing the experiment in cycles of gold deposition on poly(*N*-vinylcarbazole) (PVK) and subsequently recording the GISAXS data. The 2D GISAXS patterns are simulated, and morphological parameters of the gold film on PVK such as the cluster size, shape, and correlation distance are extracted. For the quantitative description of the cluster size evolution, scaling laws are applied. The time evolution of the cluster morphology is explained with a growth model, suggesting a cluster growth proceeding in four steps, each dominated by a characteristic kinetic process: nucleation, lateral growth, coarsening, and vertical growth. A very limited amount of 6.5 wt % gold is observed to be incorporated inside a 1.2-nm-thick enrichment layer in the PVK film.

KEYWORDS: thin film • in situ growth • conducting polymer • GISAXS • film morphology

INTRODUCTION

Vacuum-deposited metal clusters and thin films play an important role in various fields of technology (1–7). Of particular interest are metallized polymers, which are widespread used for decoration purposes, as diffusion barriers in food packaging, or as dielectric layers in microelectronics (8–12). In recent years, a new application for metallized polymer films has emerged in the fast-developing field of organic electronics. Here, a thin metal film is used to apply electrical contact to the active layer of the electronic device. Numerous types of organic transistors (13), organic light-emitting diodes (14), and organic solar cells (15) have already been realized, and although all-organic devices are also an object of intensive research (16), the use of a thin metal film as an electrode is still state-of-the-art. Next to frequently used small organic molecules like dyes from the phthalocyanine family (17), a number of conjugated polymers have also been applied, among them poly(*p*-phenylenevinylene) derivatives (18), poly(3-hexylthiophene) (19), and poly(*N*-vinylcarbazole) (PVK) (20), all showing interesting conduction behavior. Because of its thermal and chemical stability and its ability to form charge-transfer complexes (21), PVK is of particular interest for use in organic electronic devices (22).

Regardless of the polymer and metal used, an important concern in metal coatings are the interactions occurring at the metal−polymer interface because characteristics like film adhesion and electrical contact properties are strongly influenced by the interface structure. Related to this is the question for the growth kinetics of the metal film on the polymer surface and how the polymer influences the metal film morphology in the initial growth stage. Because of their nonwetting behavior, vapor-deposited metals grow on most oxide and organic surfaces in the form of 3D islands rather than in a monolayer-by-monolayer mode (23). For several combinations of oxide surfaces and metals, also a pseudo-layer-by-layer growth model has been inferred, explaining the deviation from pure 3D growth by kinetic limitations (24). A number of parameters are involved in the growth process, such as electronic structures and surface free energies of the two materials, surface morphology, polymer chain mobility, and experimental deposition conditions, determining the size, shape, and atomic structure of the metal clusters and the respective temporal correlations. In turn, film morphology influences the characteristics of the interface and, consequently, the response of the whole system. In the initial stage of film growth, metal atoms can diffuse easily into the polymer and form embedded clusters, presupposing that the deposition temperature is close to or above the glass transition temperature of the polymer (25, 26). Interdiffusion at the interface is in favor of a high adhesion strength (27); in contrast, penetrating metal atoms may alter the electronic properties at the interface and therefore make it difficult to control the properties of an electronic device (28).

For the in situ study of thin film growth and characterization of growth kinetic processes, X-rays are a powerful tool (5, 29, 30). The advanced technique of grazing incidence small-angle X-ray scattering (GISAXS) combines the advantages of small-angle scattering with the application of a grazing incidence geometry, making it a surface-sensitive tool for the study of the size, shape, and arrangement of

* E-mail: muellerb@ph.tum.de.
Received for review September 23, 2008 and accepted November 14, 2008
[†] Technische Universität München.
[‡] HASYLAB at DESY.
DOI: 10.1021/am8000727

nanoparticles in thin films (31, 32). The recorded scattering signal is an average over a macroscopic sample area, yielding an excellent sampling statistics. In combination with a dedicated UHV setup, GISAXS can be applied in situ for real-time monitoring of the cluster growth in vapor deposition processes (26, 33, 34). This allows an exact study of the kinetic growth processes at the metal–substrate interface and the derivation of the temporal correlations of structural parameters such as the cluster size, shape, and spatial distribution with the deposited metal amount, which is a prerequisite for tuning of system properties like film adhesion or band alignment at metal–organic interfaces in organic electronic devices.

EXPERIMENTAL SECTION

Sample Preparation. Glass slides were used as substrates and cleaned before coating in an acidic bath for 15 min (35). Then the substrates were rinsed with deionized water and dried in a nitrogen flow. The poly(*N*-vinylcarbazole) (PVK) layer was prepared by using the spin-coating technique. PVK with a number-average molecular weight of 290 000 g/mol and a polydispersity of 2.8 was purchased from Sigma-Aldrich and dissolved in toluene in a concentration of 2.16 mg/mL under permanent stirring. The solution was then spin-coated with a Süss MicroTec Delta6 RC spin coater under ambient conditions with 2000 rpm for 120 s. The resulting thickness of the PVK film was determined to be 10.6 nm.

GISAXS Measurements. The grazing incidence small-angle X-ray scattering (GISAXS) experiment was performed at beamline BW4 at HASYLAB (DESY, Hamburg, Germany). For in situ measurements, the beamline was equipped with a mobile UHV sputter deposition system, which is described in detail elsewhere (36). The direct current magnetron sputtering chamber was operated under an argon pressure of 5×10^{-3} mbar with a power of 3 W. By use of an additional shielding mask, a nominal deposition rate of 0.43 nm/min was realized. This low deposition rate was chosen to accurately control the growth process and to monitor its evolution with high precision. The sample was placed horizontally in the UHV deposition chamber with the surface pointing to the bottom and not heated during deposition. Prior to each deposition step, the gold target was presputtered for 5 s to remove impurities.

Figure 1 shows the principle of the GISAXS experiment. A well-collimated beam is directed to the surface of the sample under a grazing angle α_i on the order of the critical angle for the total external reflection and scattered by an assembly of particles. To the first order, the scattered intensity is proportional to the square of the particle form factor $F(q)$ times an interference function $S(q)$, where $F(q)$ is the Fourier transform of the particle shape and $S(q)$ is the Fourier transform of the particle–particle pair correlation function describing the particle assembly. Recorded on a 2D detector, the scattering pattern shows characteristic features, referring uniquely to particle assembly in real space.

The measurements were done at an X-ray wavelength of 0.138 nm and a sample-to-detector distance of 1.88 m. A setup of high-quality entrance slits for the precise limitation of the beam divergence in and out of the plane of reflection and a mostly evacuated pathway were used. A moderate microbeam focusing was achieved by using beryllium compound refractive lenses (beam size 60 μm × 30 μm) (37). For the incidence angle, a value of 0.769° well above the critical angle of gold was chosen to penetrate the full film. The scattering signal was recorded with a 2D detector, a MAR CCD camera with 2048 × 2048 pixels with 79 μm size per pixel. In front of the detector, two separate beamstops were installed at the position of the direct beam and the specular peak to shield the detector. A third rodlike beamstop was used to block the intense scattering along the plane of incidence. Deposition and GISAXS measurement were done in a stop-sputtering mode: First, the sample was coated for 60 s, corresponding to deposition of the gold amount of a 0.43-nm-thick layer. Then, a GISAXS image was recorded to a preselected maximum number of counts. After the image was taken, the same amount of gold was deposited again and the next image was recorded. The data acquisition time varied from 600 s for the uncoated polymer film and the very first gold deposition cycle to 60 s for the final images with a high gold amount deposited. In total, 49 cycles with 60 s deposition were carried out; hence, 50 individual GISAXS scattering patterns were collected to monitor the gold cluster growth. In a subsequent final step, the sample was coated for 1800 s consecutively to achieve a layer thickness as is needed in a typical electronic device.

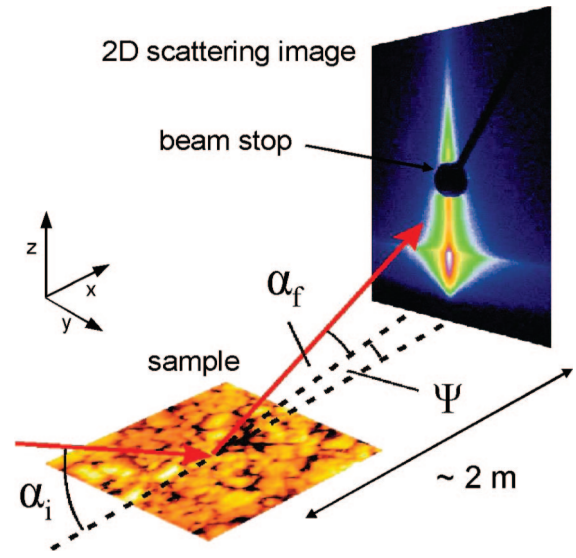

FIGURE 1. Schematic view of the GISAXS setup. The sample is illuminated with the X-ray beam under a grazing angle α_i, and the intensity is scattered by an assembly of nanosized particles. The scattered intensity is recorded on a 2D detector with dependence on two angles α_f and Ψ, corresponding to momentum transfer in the q_z, q_x, and q_y directions.

To analyze the 2D scattering data quantitatively, line profiles were extracted by taking cuts in the horizontal (q_y) and vertical (q_z) directions (with respect to the sample surface) at $\alpha_f = 0.48°$ and $\Psi = 0°$, respectively. The cuts along the q_y direction contain the information about lateral structural characteristics such as the particle size and center-to-center distance, while the cuts along the q_z direction provide information about dimensions perpendicular to the sample surface such as the particle height. All cuts were integrated over a limited q range to improve statistics.

Modeling. Data analysis is based on the software *IsGISAXS* dedicated for the simulation of GISAXS scattering patterns (38–40). By use of an appropriate model containing all relevant information about the geometry, spatial dimensions, and distribution of an arrangement of nanoparticles, either line cuts or whole 2D scattering patterns can be calculated. For form factor calculation, the distorted-wave Born approximation was used, with the assumption of graded interfaces in the perturbated state induced by the particles. Each particle type was described by parameter size, height, and orientation and their respective distributions. For all distributions, Gaussian shapes of the distribution functions were assumed. The interference function was calculated based on the 1D paracrystal model, which is a regular 1D lattice with loss of long-range order induced by a special cumulative disorder. The interference

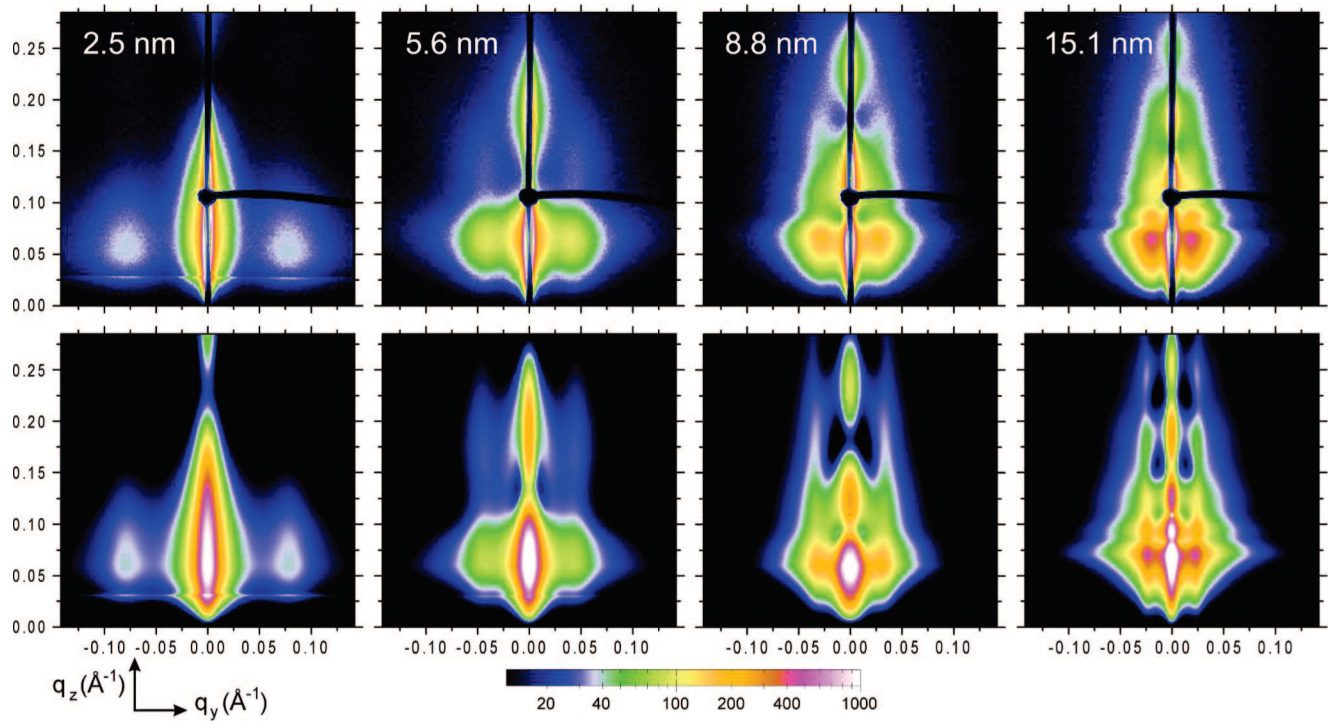

FIGURE 2. Composite image of four representative measured GISAXS scattering patterns (upper row) and corresponding simulations (lower row). The images were taken after deposition of gold layers with thicknesses of 2.5, 5.6, 8.8, and 15.1 nm. The elongated dark line in the middle of the measured images is the rodlike beamstop and the single spot the pointlike beamstop to shield the specular beam.

function was described by two parameters, the mean distance of the maxima D and the disorder parameter ω. Again, a Gaussian distribution was assumed.

Atomic Force Microscopy (AFM). Using a PARK Autoprobe CP research instrument, the sample surface was probed. All measurements were performed in noncontact mode in ambient air. Gold-coated silicon cantilevers (Ultralever cantilevers) were used, which have a resonance frequency of 60 kHz, a tip with a high aspect ratio, and an asymptotic conical shape. The radius of curvature of the tip was ≅10 nm, which is small compared to those of the structures measured. The amplitude of the oscillation of the tip was calibrated with respect to the vertical position of the piezoelectric scanner. The distance calibration of the piezocontroller was performed with a standard gold grating. Each scanned micrograph consists of 265 lines, scanned with 1.0 Hz. Scans of an area 1 μm × 1 μm in size were taken. Several images were measured for each sample. Micrographs were recorded at different sample positions.

X-ray Reflectometry. Reflectivity data were taken on a Siemens D5000 diffractometer at a wavelength of 0.154 nm (Cu Kα radiation) in an angular range from 0° to 6°. A knife edge was used for beam size limitation and background reduction.

RESULTS

In Situ GISAXS Measurements. From the recording of the full 2D GISAXS scattering patterns and subsequent modeling, detailed information about the gold cluster growth was obtained. Figure 2 shows four selected GISAXS scattering patterns, taken at gold films with 3.4, 6.5, 9.9, and 16.7 nm thickness. The scattering patterns show several prominent features evolving with the proceeding gold deposition. The most prominent feature in the GISAXS patterns is a side peak emerging at larger scattering angles and, with proceeding growth of the gold clusters, shifting towards smaller values. The peak is related to a maximum in the interference function describing the cluster correlation distance. The shifting therefore represents a change in the relative cluster position, i.e., an increasing center-to-center distance. Further well-pronounced features in the GISAXS patterns are the higher order scattering maxima evolving in the vertical direction, indicating a nearly uniform height of the clusters with only small variances. From the scattering maxima in the horizontal direction arise weak streaks bending to the plane of reflection and connecting the lateral maxima with vertical maxima. These streaks originate from a round shape of the clusters, as it is also expected from the nonwetting behavior of gold on polymer surfaces (41). Consequently, a 3D cluster growth (Volmer−Weber growth) is preferred over a 2D layer-by-layer growth (Frank−Van der Merwe growth) expected for the wetting case.

For comparison, the 25-nm-thick gold layer after complete deposition and a PVK surface without gold deposition were measured with AFM (see Figure 3). The image of the gold film shows a rough surface consisting of gold clusters of a round, but not necessarily circular, shape. The clusters are homogeneous in size with a diameter of about 50 nm. Only a few clusters are considerably larger. The film structure is dense, and no interspaces between adjacent clusters with a depth on the order of the cluster height are visible; i.e., the PVK surface is fully covered. However, a direct comparison between AFM and GISAXS is not easy because, on the one hand, AFM was not measured in situ and, on the other hand, with AFM the very final deposition state was probed. As compared to the final state probed with GISAXS, this very final state has a 10-nm-thicker gold layer deposited.

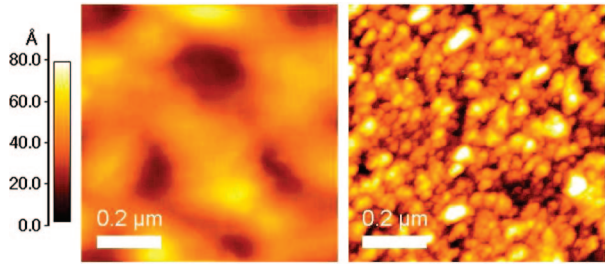

FIGURE 3. AFM images showing the surface of a bare PVK film (left) and of the 25-nm-thick gold layer after complete deposition (right). The surface roughness of the PVK is reproduced by the gold layer, and the gold clusters are homogeneous in size and height.

In comparison with the image of the uncoated PVK film, the surface roughness of the PVK is replicated by the gold layer; the larger-scale height variations present in the gold surface are also found in the surface of the PVK film. This confirms the uniform height growth of the gold clusters concluded from the GISAXS images even at the very final state.

Simulation of the Scattering Patterns. Figure 2 shows the 2D simulated scattering patterns together with the corresponding measured data. For modeling, different particle geometries such as spheroids, truncated spheres, cylinders, and parallelepipeds were tried. The best agreement was obtained by use of the parallelepiped geometry, in particular in the description of the intensity distribution of the side peaks. Because the interconnecting streaks in the measured data suggest a round shape of the clusters, a second particle geometry, spheroids, was introduced in the model. The particles of both geometries are arranged statistically with an equal probability of occurrence of 0.5 for each site. In this case, the form factor is an incoherent sum of the respective particle contributions, and the overall intensity is calculated by use of one interference function describing the assembly of the particles independently of their geometry. Only one average radius value was used in the calculations and assigned to both the parallelepiped and spheroid particles; to account for shape variations, only the radius distribution width was used for fitting. The height of the spheroid particles turned out to be slightly higher than the height of the parallelepiped particles, yielding almost the same volume for the particles of both geometries. With this two-particle-type model, a distinctly better quality of the simulations was obtained. In particular, the archlike streaks connecting the scattering maxima in horizontal and vertical directions are extremely well described. Table 1 summarizes the morphological parameters used for the simulations shown in Figure 2. In the following, these modeled gold particles are referred to as clusters for simplification.

The modeling procedure described above was applied to all 2D GISAXS scattering patterns to follow the temporal evolution of the cluster size and spatial distribution. The resulting values of the cluster height, radius, and correlation distance are shown in Figure 4 as a function of the effective film thickness. This effective film thickness equals a rescaled deposition time, where the specific deposition conditions are taken into account. For the cluster height, a nonlinear

Table 1. Morphological Parameters Extracted from Simulation of the Data by Use of a Model Consisting of Parallelepiped and Spheroid Particle Geometries To Describe the Cluster Shape[a]

t (min)	d_0 (nm)	d (nm)	r_p (nm)	σ_p (nm)	h_p (nm)	r_s (nm)	σ_s (nm)	h_s (nm)	D (nm)	ω (nm)
9	3.9	2.5	4.8	20.0	3.6	4.8	11.0	4.3	11.8	3.8
19	8.2	5.6	9.1	22.5	6.1	9.1	5.3	6.8	19.0	7.2
29	12.5	8.8	13.5	17.6	8.8	13.5	14.9	9.9	27.0	10.2
49	21.1	15.1	20.0	36.0	15.2	20.0	18.0	16.4	40.0	15.2

[a] t is the deposition time, d_0 denotes the film thickness expected from the nominal deposition rate (0.43 nm/min) and d the observed value, r_p, σ_p, and h_p are the radius and radius distribution width and height of the parallelepipeds and r_s, σ_s, h_s the respective values of the spheroids, D is the correlation distance, and ω is the disorder parameter for D.

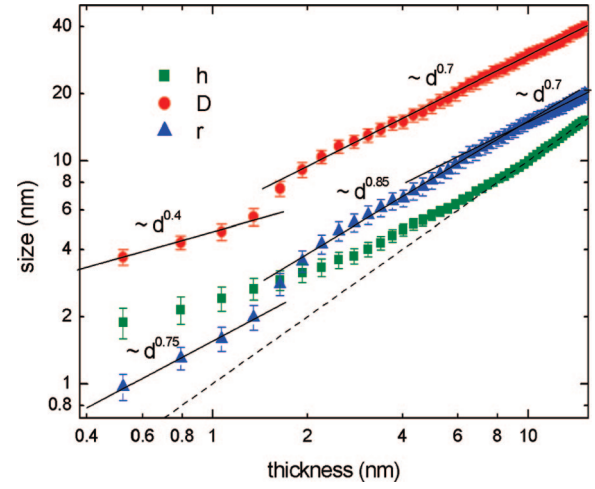

FIGURE 4. Evolution of the cluster height (parallelepiped geometry, squares), radius (triangles), and correlation distance (circles) with gold deposition. The dashed line marks the film thickness, which is lower than the cluster height in the initial growth stage because of the 3D cluster growth. For the lateral cluster dimensions, distinct growth regimes with different scaling laws are distinguishable.

progress with the deposited gold amount is obvious. Up to a value of 9 nm, the cluster height exceeds the film thickness, proving the 3D growth mode with pronounced height growth in the early stage of cluster formation. Furthermore, a deviation between the cluster height and film thickness expected from the nominal deposition rate (0.43 nm/min) is noticeable. The experimentally determined values are only about $^3/_4$ of the expected values (see Table 1 for comparison). An explanation for this behavior might be a reduced condensation coefficient on the gold surface, eventually caused by direct reevaporation of high-energy particles. From the linear part in the cluster height plot, a real deposition rate was derived. The best fit yields a rate of 0.32 nm/min, with an offset of −0.55 nm. This offset originates from a further reduced condensation coefficient for gold particles on the PVK surface. In general, the condensation coefficients of metals on polymers are significantly lower than 1, whereas extreme values below 0.01 and close to 1 have been found as well (42).

From the cluster height h and the effective film thickness d, the surface coverage ε was calculated by using the relation

$$\varepsilon = d/h \quad (1)$$

To account for the reduced condensation coefficient of gold on PVK, an exponential approach of the deposition rate to the derived value of 0.32 nm/min was introduced for the calculation of d. Figure 5 shows the resulting surface coverage and the correlation with film thickness. At a thickness of 9 nm, the maximum surface coverage is reached and the polymer surface is completely covered with a gold layer. To further quantify the correlation with the deposited gold amount, the data were fitted with an exponential approach function

$$\varepsilon = 1 - \exp[-(d/\delta)^m] \quad (2)$$

where the best fit was obtained with a characteristic constant $\delta = 2.02$ nm and a scaling exponent $m = 0.87$. This reduced exponential growth might be an effect of the complex diffusion and coalescence mechanisms governing the cluster structure formation, resulting in a deviation from pure exponential growth.

To rule out significant diffusion of gold into the polymer, an additional X-ray reflectivity measurement was done at the film after complete deposition (Figure 6). The large difference in the electron densities of gold and PVK makes this method sensitive to small amounts of metal incorporated in the PVK layer. This effect is further accentuated by the low thickness of the polymer film. The measurements revealed the formation of a gold enrichment layer in the PVK film with a thickness of 1.2 nm and a mass density of 2.4 g/cm^3 (the value for PVK is 1.2 g/cm^3 for comparison), corresponding to a gold incorporation of 6.5 wt % or an amount of less than 0.1 monolayer, respectively. The investigation methods as applied allow no statement whether the gold is present in the PVK layer in the form of diffused single atoms or sinked small clusters or about the temporal progress of the penetration process. Nevertheless, it must be stated that penetration of gold into the PVK film under the chosen deposition conditions is present and might be of importance for applications. Because of its inert character, gold is not expected to react with the polymer and to form covalent bonds with either the backbone or the side chains, but a charge transfer between incorporated gold atoms and the polymer can occur and "dope" the polymer, resulting in an altered Fermi level at the metal/polymer interface. This, in turn, has a strong influence on the response of a device, e.g., in a reduced electron injection barrier (43).

On the basis of surface coverage ε and correlation distance D, the cluster radius was calculated by assumption of the parallelepiped geometry:

$$r = \frac{1}{2} D\sqrt{\varepsilon} \quad (3)$$

The radius increases continuously with the deposited gold amount (Figure 4). A similar behavior shows the correlation distance, indicating a cluster growth with permanent coalescence. Three distinct growth regimes with different scaling laws $D \sim d^{\alpha}$ and a transition in between are distinguished. In the initial stage, the cluster radius scales with $\alpha_r = 0.75$ and the correlation distance with $\alpha_d = 0.40$. A transition point occurs at 1.3 nm; later on, the radius scaling is well described by $\alpha_r = 0.85$ and the correlation length

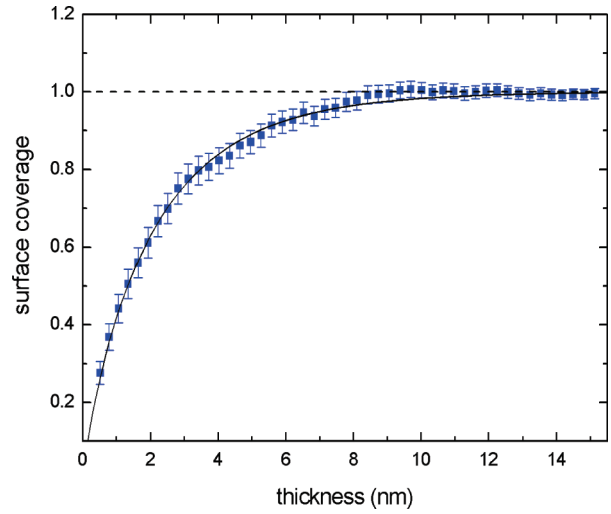

FIGURE 5. Surface coverage calculated from the cluster height and effective film thickness as a function of the effective film thickness. The solid line is a fit to the data with an exponential approach function $\varepsilon = 1-\exp[-(d/\delta)^m]$ with $\delta = 2.02$ nm and $m = 0.87$.

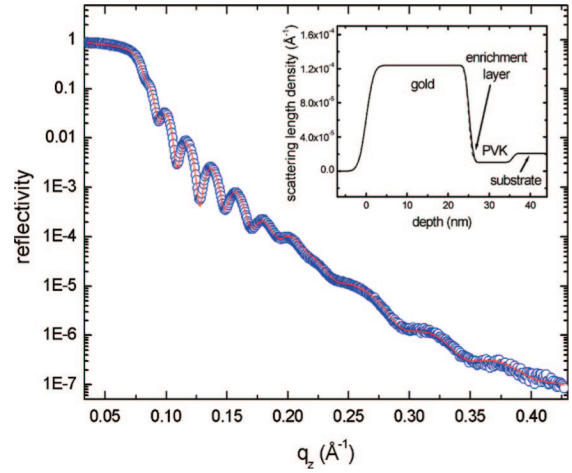

FIGURE 6. Measured reflectivity curve of the PVK film coated with 25 nm gold (circles) and fit to the data (solid line). The inset shows the scattering length density profile calculated from the fit including a 1.2-nm-thick enrichment layer with 6.5 wt % gold incorporation in the PVK. Because of the roughness of the gold–PVK interface, the enrichment layer is spread over a depth range of several nanometers and appears only as a weak shoulder in the scattering length density profile. For clarification, the dashed line shows the profile without the enrichment layer.

scaling by $\alpha_d = 0.7$. For the radius scaling, a second transition occurs at an effective film thickness of 9 nm, the point where complete surface coverage is reached. Afterward, the radius scaling is identical with the correlation distance scaling ($\alpha_r = 0.7$).

A detailed explanation for these observations will be given in the following section in the framework of a growth model consisting of four growth stages.

GROWTH MODEL

The results obtained from simulation of the scattering data suggest a cluster growth process proceeding in four stages, with a characteristic kinetic process assigned to each stage.

1. Nucleation Stage. This first step of cluster growth comprises the initial stage of deposition with a gold deposit

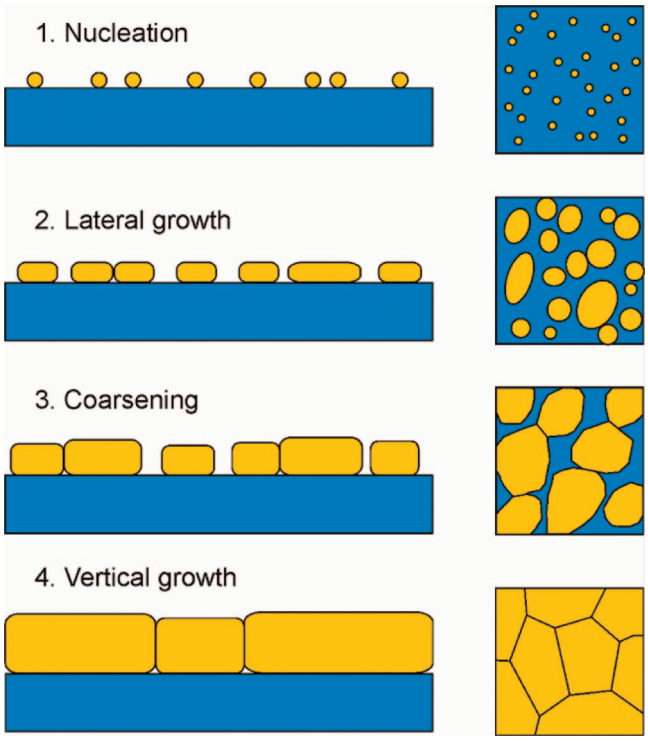

FIGURE 7. Schematic drawing of gold cluster growth. After the stage of nucleation, cluster growth proceeds mainly in the lateral direction. Coarsening sets in and becomes the dominating process when the surface coverage increases and the clusters get in close contact with each other. With the surface fully covered, adsorption produces only vertical growth and lateral growth is dominated by cluster boundary motion.

of less than one monolayer. Under the deposition conditions used, this amount is achieved in a time of less than 1 min; thus, the process is covered completely by the first deposition cycle. However, the processes determining the gold cluster growth in this stage are well-known, and some conclusions can be derived using the literature (44, 45).

When a gold atom impinges on the PVK surface, it is adsorbed and diffuses laterally along the surface. The chemical bond to the polymer chains is weak and the adatom can desorb again easily, which is expressed in the observed condensation coefficient being lower than 1. In competition with desorption is the formation of stable nuclei where two or more adatoms join. Once stable nuclei have formed, diffusing adatoms can be captured and the nuclei grow in size to small clusters. To minimize the interface with the polymer, the clusters adopt a spherical or ellipsoidal shape, with the height being a multiple of the film thickness (3D growth). The surface coverage remains low at this stage. Nucleation continues until a maximum number density of nuclei is reached, where the probability for a diffusing adatom to be captured by an existing cluster is much higher than that for it to join with a second adatom to a new nucleus (Figure 7).

2. Lateral Growth Stage. Once the critical cluster density is reached, nearly all impinging atoms are captured by the present gold clusters and only a few new nuclei form. A distinctive lateral growth starts by adsorption of diffusing adatoms, and the surface coverage increases rapidly. This process is amplified by an increase in the condensation coefficient resulting from the higher portion of gold-covered surface and a simultaneously decreasing distance that adatoms have to travel to reach a cluster before desorption (44). At a point where two clusters get in close contact with each other, coalescence occurs and a larger cluster is formed. As long as the cluster size is small, the cluster mobility is high enough to allow the clusters to travel along the surface and to approach other clusters, resulting in permanent diffusion-driven coalescence, a process similar to post-deposition Smoluchowski ripening (46).

The evolution of the cluster radius in this stage is well described by a power law with a scaling exponent $\alpha_r = 0.75$. A similar value was found for the growth of coalescing water droplets under permanent vapor flux (47) and later also reported for the growth of solid nanoparticles (33). The scaling exponents for the radius and correlation distance in this stage, $\alpha_r = 0.75$ and $\alpha_d = 0.40$, are in well accordance with the relation $\alpha_r = \alpha_a + \alpha_d$, if $\alpha_a = {}^1/_3$ is the scaling exponent for adsorptive growth without coalescence (48).

Because lateral growth is proceeding fast and the time is not sufficient to recover the full equilibrium shape, which holds in particular in the case of coalescence, the clusters start to lose their regular shape and become elongated or assume a polygonal shape.

3. Coarsening Stage. At an effective thickness of 1.3 nm, a transition point is reached, where the clusters have grown to a size in which the mean diameter is close to the mean correlation distance between two clusters; i.e., the clusters are in close contact with each other. Now coalescence is no longer dependent on migration, and the clusters grow rapidly in size; the same holds for the distance. A similar effect was observed for the growth of copper clusters on highly ordered pyrolytic graphite (49) and explained by an absence of interaction with the surface allowing a high degree of cluster mobility. When the clusters grow in size, the time needed for full coalescence is longer, resulting in an immediate self-amplified slowing down of the coalescence process. At this stage, the cluster radius scales with $\alpha_r = 0.85$ and the correlation distance with $\alpha_d = 0.7$, proving that coalescence, nevertheless, remains a dominant and fast-proceeding process. From the uncovered surface portion, adatoms still adsorb to clusters and support lateral growth, until the fully covered surface is reached at a film thickness of 9 nm. The polygonal shape of the clusters is now well pronounced because of the constraint of full surface coverage.

4. Vertical Growth Stage. After a fully covered surface is reached (coverage of 1), adsorptive growth proceeds only in the vertical direction and the cluster height equals the film thickness. Lateral coarsening continues, now mainly driven by the motion of cluster boundaries instead of the motion of whole clusters, a process well-known as grain growth. The radius scales in this stage with $\alpha_r = 0.7$, the same value as that for the scaling of the correlation distance, in accordance with a densely packed structure in which the mean size equals the mean distance. In the final state, the clusters have grown to a continuous layer with a

polycrystalline grain structure characteristic of vapor-deposited thin films (50).

CONCLUSIONS

In this study, GISAXS was used to follow the growth of a thin gold film on a conducting polymer film from nucleation to formation of a continuous layer. The GISAXS data were modeled to describe the cluster geometry and to extract the morphological parameters radius, height, and correlation distance. This not only allows one to follow the time-resolved cluster growth and to derive a growth model to understand the kinetic processes governing cluster growth but also provides the possibility for cluster growth control. Once the correlations between the deposited amount and cluster morphology are known, taking into account the material characteristics of the substrate and deposit, clusters of a specific size and shape can be prepared. With increasing application of nanosized structures, the need for precise preparation with morphology control also increases, requiring an exact knowledge of growth processes and the underlying basic principles.

The morphology evolution of the gold clusters extracted from the simulations suggests a growth proceeding in four major steps, where each step is dominated by a characteristic kinetic process. After the initial stage of nucleation, the clusters grow laterally under permanent coalescence until a state with dense distribution is reached. Coarsening is then temporarily enhanced, while full surface coverage on the film mainly grows in the vertical direction. Coalescence turned out to occur over the whole deposition process, playing the major role in the formation of the lateral cluster structure and determining the grain structure in the continuous film.

During deposition, a small amount of gold diffused into PVK and formed an enrichment layer at the interface. With an absolute amount of less than 0.1 monolayer incorporated gold atoms, the influence on cluster growth is negligible for the gold−PVK system under the chosen deposition conditions. Nevertheless, diffusion of gold atoms inside the PVK film might be of importance in electronic applications. The incorporated gold can act as a sort of doping to the conducting polymer layer, in terms of tuning of the electrical properties of the interface to an optimal response.

Although plenty of experiments studying cluster growth have been done in the past, the covered period in most cases was limited to the initial growth stage up to a deposit of several monolayers. Here, we went further, intending to understand the basic processes continuing over the whole growth process and how the structure observed in later stages of vapor deposition is related to the stage of cluster growth.

Acknowledgment. We thank A. Timmann for his help in the setup of the BW4 beamline. B. Russ and P. Böni supported us in the reflectivity experiments. Financial support by DFG in the priority program SPP 1181 (MU1487/5) and by the International Graduate School 'Materials Science of Complex Interfaces' (CompInt) is gratefully acknowledged.

REFERENCES AND NOTES

(1) Biswas, A.; Karulkar, P. C.; Eilers, H.; Norton, M. G.; Skorski, D.; Davitt, C.; Greve, H.; Schürmann, U.; Zaporojtchenko, V.; Faupel, F. *Vac. Technol. Coat.* **2006**, *7*, 54.
(2) Bauer, G.; Hassmann, J.; Walter, H.; Haglmüller, J.; Mayer, C.; Schalkhammer, T. *Nanotechnology* **2003**, *14*, 1289.
(3) Ditlbacher, H.; Krenn, J. R.; Lamprecht, B.; Leitner, A.; Aussenegg, F. R. *Opt. Lett.* **2000**, *25*, 563.
(4) Hynninen, A.; Thijssen, J. H. J.; Vermolen, E. C. M.; Dijkstra, M.; Blaaderen, A. V. *Nat. Mater.* **2007**, *5*, 605.
(5) Roth, S. V.; Walter, H.; Burghammer, M.; Riekel, C.; Lengeler, B.; Schroer, C.; Kuhlmann, M.; Walther, T.; Sehrbrock, A.; Domnick, R.; Müller-Buschbaum, P. *Appl. Phys. Lett.* **2006**, *88*, 021910.
(6) Westphalen, M.; Kreibig, U.; Rostalski, J.; Lüth, H.; Meissner, D. *Sol. Energy Mater. Sol. Cells* **2000**, *61*, 97.
(7) Stenzel, O.; Stendal, A.; Voigtsberger, K.; von Borczyskowski, C. *Sol. Energy Mater. Sol. Cells* **1995**, *37*, 337.
(8) Takele, H.; Jebril, S.; Strunskus, T.; Zaporojtchenko, V.; Adelung, R.; Faupel, F. *Appl. Phys. A* **2008**, *92*, 345.
(9) Hanisch, C.; Kulkarni, A.; Zaporojtchenko, V.; Faupel, F. *J. Phys.: Conf. Ser.* **2008**, *100*, 052043.
(10) Hajati, S.; Zaporojtchenko, V.; Faupel, F.; Tougaard, S. *Surf. Sci.* **2007**, *601*, 3261.
(11) Takele, H.; Schürmann, U.; Greve, H.; Paretkar, D.; Zaporojtchenko, V.; Faupel, F. *Eur. Phys. J.: Appl. Phys.* **2006**, *33*, 83.
(12) Erichsen, J.; Kanzow, J.; Schürmann, U.; Dolgner, K.; Günther-Schade, K.; Strunskus, T.; Zaporojtchenko, V.; Faupel, F. *Macromolecules* **2006**, *37*, 1831.
(13) Muccini, M. *Nat. Mater.* **2006**, *5*, 605.
(14) Mitschke, U.; Bäuerle, P. *J. Mater. Chem.* **2000**, *10*, 1471.
(15) Hoppe, H.; Sariciftci, N. S. *J. Mater. Res.* **2004**, *19*, 1924.
(16) Shibata, K.; Wada, H.; Ishikawa, K.; Takezoe, H. *Appl. Phys. Lett.* **2007**, *90*, 193509.
(17) Blochwitz, J.; Pfeiffer, M.; Fritz, T.; Leo, K. *Surf. Sci. Rep.* **1998**, *73*, 729.
(18) Zhang, F. L.; Johansson, M.; Andersson, M. R.; Hummelen, J. C.; Inganäs, O. *Synth. Met.* **2003**, *137*, 1401.
(19) Ma, W.; Yang, C.; Gong, X.; Lee, K.; Heeger, A. *J. Adv. Mater.* **2005**, *15*, 1617.
(20) Ouro Djobo, S.; Bernèdea, J. C.; Napob, K.; Guellil, Y. *Mater. Chem. Phys.* **2003**, *77*, 476.
(21) Pearson, J. M.; Stolka, M. *Poly(N-vinylcarbazole)*; Gordon and Breach: New York, 1981.
(22) Kaune, G.; Wang, W.; Metwalli, E.; Ruderer, M.; Rossner, R.; Roth, S.; Müller-Buschbaum, P. *Eur. Phys. J. E* **2008**, *26*, 73.
(23) Campbell, C. T. *Surf. Sci. Rep.* **1997**, *27*, 1.
(24) Ernst, K. H.; Ludviksson, A.; Zhang, R.; Yoshihara, J.; Campbell, C. T. *Phys. Rev. B* **1993**, *47*, 13782.
(25) Strunskus, T.; Kiene, M.; Willecke, R.; Thran, A.; von Bechtolsheim, C.; Faupel, F. *Mater. Corros.* **1998**, *49*, 180.
(26) Metwalli, E.; Couet, S.; Schlage, K.; Röhlsberger, R.; Körstgens, V.; Ruderer, M.; Wang, W.; Kaune, G.; Roth, S. V.; Müller-Buschbaum, P. *Langmuir* **2008**, *23*, 4265.
(27) Silvain, J. F.; Veyrat, A.; Ehrhardt, J. J. *Thin Solid Films* **1992**, *221*, 114.
(28) Seki, K.; Hayashi, N.; Oji, H.; Ito, E.; Ouchi, Y.; Ishii, H. *Thin Solid Films* **2001**, *393*, 298.
(29) Alvarez, J.; Lundgren, E.; Torrelles, X.; Ferrer, S. *Phys. Rev. B* **1998**, *57*, 6325.
(30) Sun, T.; Hu, H.; Pan, Z.; Li, X.; Wang, J.; Dravid, V. P. *Phys. Rev. B* **2008**, *77*, 205414.
(31) Müller-Buschbaum, P. *Anal. Bioanal. Chem.* **2003**, *376*, 3.
(32) Perlich, J.; Memesa, M.; Diethert, A.; Metwalli, E.; Wang, W.; Roth, S. V.; Timmann, A.; Gutmann, J. S.; Müller-Buschbaum, P. *Chem. Phys. Chem.* **2008**, submitted for publication.
(33) Renaud, G.; Lazzari, R.; Revenant, C.; Barbier, A.; Noblet, M.; Ulrich, O.; Leroy, F.; Jupille, J.; Borensztein, Y.; Henry, C. R.; Deville, J.-P.; Scheurer, F.; Mane-Mane, J.; Fruchart, O. *Science* **2003**, *300*, 1416.
(34) Jedrecy, N.; Renaud, G.; Lazzari, R.; Jupille, J. *Phys. Rev. B* **2005**, *72*, 045430.
(35) Müller-Buschbaum, P. *Eur. Phys. J. E* **2003**, *12*, 443.
(36) Couet, S.; Diederich, T.; Schlage, K.; Röhlsberger, R. *Rev. Sci. Instrum.* **2008**, *79*, 093908.

(37) Roth, S. V.; Döhrmann, R.; Dommach, M.; Kuhlmann, M.; Kröger, I.; Gehrke, R.; Walter, H.; Schroer, C.; Lengeler, B.; Müller-Buschbaum, P. *Rev. Sci. Instrum.* **2006**, *77*, 085106.
(38) Lazzari, R. *J. Appl. Crystallogr.* **2002**, *35*, 406.
(39) Lazzari, R.; Leroy, F.; Renaud, G. *Phys. Rev. B* **2007**, *76*, 125411.
(40) Lazzari, R.; Renaud, G.; Jupille, J.; Leroy, F. *Phys. Rev. B* **2007**, *76*, 125412.
(41) von Bechtolsheim, C.; Zaporojtchenko, V.; Faupel, F. *Appl. Surf. Sci.* **1999**, *151*, 119.
(42) Zaporojtchenko, V.; Behnke, K.; Thran, A.; Strunskus, T.; Faupel, F. *Appl. Surf. Sci.* **1999**, *144–145*, 355.
(43) Kahn, A.; Koch, N.; Gao, W. *J. Polym. Sci., Part B: Polym. Phys.* **2003**, *41*, 2529.
(44) Venables, J. A.; Spiller, G. D. T.; Hanbücken, M. *Rep. Prog. Phys.* **1984**, *47*, 399.
(45) Kukushkin, S. A.; Osipov, A. V. *Phys.—Usp.* **1998**, *41*, 983.
(46) Stoldt, C. R.; Jenks, C. J.; Thiel, P. A.; Cadilhe, A. M.; Evans, J. W. *J. Chem. Phys.* **1999**, *111*, 5157.
(47) Beysens, D.; Knobler, C. M. *Phys. Rev. Lett.* **1986**, *57*, 1433.
(48) Viovy, J. L.; Beysens, D.; Knobler, C. M. *Phys. Rev. A* **1988**, *37*, 4965.
(49) Yang, D. Q.; Sacher, E. *J. Appl. Phys.* **2001**, *90*, 4768.
(50) Thornton, J. A. *Annu. Rev. Mater. Sci.* **1977**, *7*, 239.

AM8000727